Eur. Phys. J. B **35**, 49–55 (2003)
DOI: 10.1140/epjb/e2003-00255-7

THE EUROPEAN PHYSICAL JOURNAL B

Growth atomic mechanisms of pulsed laser deposited La modified-$PbTiO_3$ perovskites

E. Vasco[a], C. Polop[b], and C. Ocal

Instituto de Ciencia de Materiales de Madrid, Consejo Superior de Investigaciones Científicas, Cantoblanco, 28049 Madrid, Spain

Received 13 February 2003 / Received in final form 18 June 2003
Published online 22 September 2003 –

Abstract. The microstructure and morphology of 100/001-oriented La modified-$PbTiO_3$ (PLT) films grown by pulsed laser deposition have been analyzed and elucidated within the framework of morphology evolution models, such as the Dynamic Scaling Theory and Structure Zone Model. The experimental results were obtained from X-ray diffraction, atomic force microscopy and cross-section scanning electron microscopy. PLT grows with a compact columnar microstructure. The columns are formed by coherently grouped grains and show oblique walls and rounded tops. Connecting the experimental results with the morphology evolution models, the growth mechanisms involved in the deposition process were identified. While inside each column, the existing Pb vacancies govern the coarsening and coalescence of the grains, a non-local effect of geometric shadowing of the incident particle flux during growth controls competition between columns and their coarsening.

PACS. 68.55.-a Thin film structure and morphology – 81.15.Fg Laser deposition – 77.84.Dy Niobates, titanates, tantalates, PZT ceramics, etc.

1 Introduction

The properties of a thin solid film are closely linked to its microstructure and especially to its morphology and surface roughness through, for instance, scattering [1] and relaxation processes [2]. Generally, these features are determined by the atomic mechanisms operating during the film growth. The knowledge of such mechanisms has motivated a large amount of studies during the last years. In particular, a great effort has been focused on the scaling studies of the morphological evolution of films grown from vapor deposition techniques [3] within the frame of the Dynamic Scaling Theory (DST) [4,5].

During film growth, the evolving surface is statistically characterized by two lengths: the interface width w (or root mean square surface roughness), and a lateral correlation length, ξ, associated with the horizontal cutoff to scaling. The theory assumes that these lengths increase with the deposition time as: $w \sim t^{\beta}$ and $\xi \sim t^{\beta/\alpha} = t^{1/z}$, being β, α and $1/z$ the growth, roughness and coarsening exponents, respectively. Furthermore, a defined set of exponents is predicted for each isolated mechanism. The theoretical predictions provided by different numerical and analytical models identify the mechanisms based on the fact that each one originates a characteristic morphological evolution of the growing surface [5]. However, the scaling approach presents severe limitations to separate mechanisms that operate at similar spatial scales as well as to reproduce the evolution of a non self-affine surface.

At the same time, other models, more phenomenological, have been extensively applied to predict the microstructure of the vapor-deposited films. This is the case of the Structure Zone Model (SZM) [6,7], which suggests that the developed microstructure is a universal function of the ratio between the deposition and melting temperatures (T_s/T_m). The SZM model explains the morphological evolution as the result of the competition between the non-local shadowing effect and the surface relaxation mechanisms, such as diffusion and surface tension. Since these latter mechanisms are thermally activated, the T_s/T_m ratio defines the magnitude of the surface relaxation capacity. Depending on the T_s/T_m ratio value, three microstructure zones are defined [6,7]: zone I ($T_s/T_m < 0.24{-}0.3$), characterized by tapered columns with domed tops separated by a high density of pores or voids; zone II ($T_s/T_m < 0.5{-}0.55$), described as a regular arrangement of uniform columns exhibiting smooth tops and diameters slightly smaller than the film thickness;

[a] *Current address*: Institut für Festkörperforschung, Forschungszentrum Jülich, 52425 Jülich, Germany
e-mail: e.vasco.matias@fz-juelich.de
[b] *Current address*: I. Physikalisches Institut, RWTH-Aachen, 52056 Aachen, Germany

and zone III ($T_s/T_m > 0.5-0.55$), formed by equiaxed grains. The SZM model has been partially modified to include the influence of the deposition pressure PO_2, besides T_s/T_m, on the resulting microstructure of films deposited in gaseous atmospheres [8].

Despite the extensive effort devoted to identify the atomic growth mechanisms operating in metallic and semiconductor systems, very few studies concerning the multicationic oxide growth are available [9,10]. This fact is surprising taking into account the increasing technological interest gathered by some of these oxides, for instance the high-T_c superconductors [11], ferroelectrics [12] and colossal magnetoresistors [13]. Especially, the number of scaling studies about oxides with high-volatile elements, among which stands out modified-$PbTiO_3$ [10], is still more reduced. La-modified $PbTiO_3$ ($Pb_{1-3/2x}\square_{x/2}La_xTiO_3$ = PLT) is particularly attractive because its piezoelectric, ferroelectric and optical properties are easily tunable through the included La proportion (x), which determines the tetragonality (c/a) of its crystalline structure [14,15]. x can be chosen in order to improve the functional properties required for a specific application. Thus, for $x = 0.15$ a large piezoelectric coefficient ($d_{33} = 82.8$ pm/V) has been found [16], while at $x \approx 0.1$ the pyroelectric properties [17] and the optical losses [18] are optimized. This makes PLT suitable for several applications such as: electro-optic material for surface acoustic wave devices and waveguides [19], pyroelectric detector [20], or capacitor and ferroelectric medium for the non-volatile memory implementation [21]. Finally, the PLT integration with direct-gap semiconductors, which are used for the implementation of optoelectronic monolithic circuits (OIC), is particularly relevant as it constitutes an effective way to incorporate the acoustic-optic interactions to OIC for optical signal processing [22].

The main goal of this work is to identify the growth mechanisms operating during the pulsed laser deposition (PLD) of La-modified $PbTiO_3$ through the study of the morphology and microstructure evolution of films grown under different deposition conditions. PLD has been shown to be a technique especially suitable for the stoichiometric deposition of multicationic oxide films [23], since the laser ablation of the target produces a congruent evaporation of the constitutive elements. The grown films were studied by Scanning electron microscopy (SEM), Atomic force microscopy (AFM) and $\theta-2\theta$ X-ray diffraction (XRD). The analysis of the microstructure has been performed within the framework of morphology evolution models (DST and SZM).

2 Experimental

PLT films with different La compositions ($x = 0.08$, 0.15 and 0.20) were deposited by PLD using a KrF excimer Laser emitting 16 ns pulses at 248 nm with a frequency of 10 Hz. The focused laser beam impacted at 45° into a reduced area (2 mm^2) of the rotating target surface (at 20 rpm) with an energy density of 4 J/cm^2. The ceramic PLT targets were prepared by solid-state reaction of $PbO/La_2O_3/Ti_2O_3$ powder mixtures, 10% weight-enriched in PbO with respect to the nominal target formula in order to avoid Pb losses. The deposition was made in a high vacuum chamber with a base pressure of 8×10^{-7} mbar. During deposition, high purity molecular oxygen (99.999%) was introduced to reach a dynamic pressure, PO_2, in the range of 0.05−0.20 mbar. Different pulsed laser deposited films on (100)InP [24] (*e.g.* cube-on-cube epitaxed (100)YSZ, 111-textured CeO_2 and 100-textured $SrTiO_3$) were employed as buffer layers. These buffer layers are commonly required to overcome several technological drawbacks concerning PLT/InP integration: a) The high PLT/InP lattice mismatch ($\approx 34\%$) hindering the PLT cube orientation. b) The rather extreme deposition conditions of PLT ($PO_2 \geq 10^{-1}$ mbar and substrate temperature $T_s \geq 600\,^{\circ}C$) [25] inducing InP surface degradation rendered by the P preferential evaporation [26] and the In reoxidation [27]. c) Metallic cations such as Pb diffusing into the semiconductor [28]. The buffer/InP substrates were placed opposite to the target at a distance of 60 mm and heated in the 823−973 K range. Changes in the morphology of PLT films due to deposition on different buffers were negligible compared to major modifications induced by variations of the deposition conditions. This suggests that the mechanisms that operate during the growth of this perovskite oxide are not significantly influenced by the buffer layers. Afterwards, data of PLT deposited on several buffers have been indistinctly used to perform this analysis. The average growth rate was in the range of 0.11−0.18 Å/pulse.

The film morphologies were characterized by AFM using a homemade setup operating in contact mode. V-shaped Si_3N_4 sharpened cantilevers with a radius of 100 Å and a nominal force constant of 0.5 N/m were used. For each sample, several AFM images with sizes ranging from 0.2×0.2 μm^2 to 10×10 μm^2 were taken at different sample zones. The root mean square roughness, w, was determined from the images with largest surface area. The power spectral density curves, $PSD(k)$, calculated as the square of the 2D Fourier transform coefficients of the digitized surface, was provided by the AFM software. Afterwards, ξ was estimated from the crossover ($k_c = 1/\xi$) of the $PSD(k)$. The crystallinity and orientation of the PLT films were studied by XRD using a D-500 Siemens diffractometer operating in $\theta-2\theta$ mode with Cu K_α radiation. The film microstructure was inspected by SEM in cleaved samples. The cross-section images were taken by means of an ICI DS-130C high scanning electron microscope operating at 20 kV. The film thicknesses were measured with a Talysurf-50 profilometer and tested by the cross-section SEM.

3 Results and discussion

3.1 Microstructure

Figure 1a shows a cross-section SEM image of an 800 nm thick PLT film ($x = 0.08$) deposited on CeO_2/InP. While, the CeO_2 buffer film appears as a compact film without special features, the PLT film shows a compact columnar

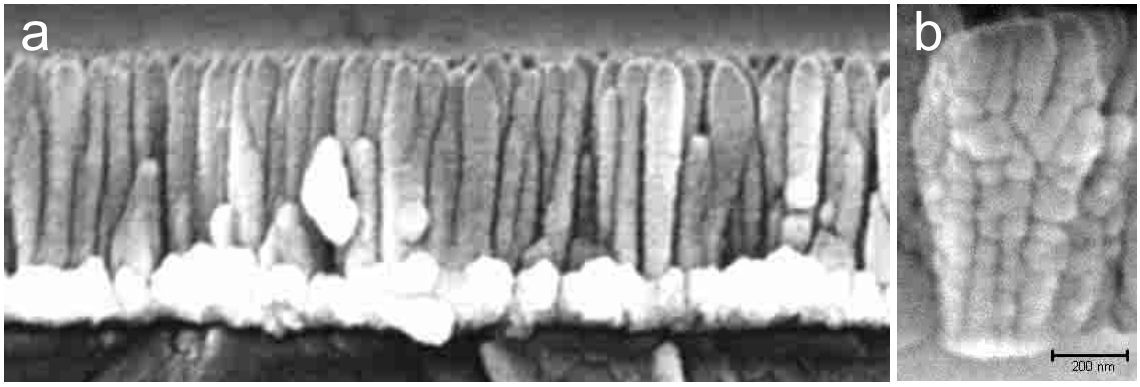

Fig. 1. a) Cross-section SEM micrograph of PLT/CeO_2/InP taken at 20 kV. The 800 nm thick PLT ($x = 0.08$) film was deposited at $T_s = 923$ K in $PO_2 = 0.1$ mbar on a 200 nm thick CeO_2 buffer layer. b) Higher resolution details of a single column in PTL(0.08)/YSZ/InP.

growth habit. The columnar growth habit of modified-$PbTiO_3$ has been previously observed [29] and related to films with preferred oriented grains and good electrical properties [30]. The columns, which extend through the entire film thickness, present round and smooth tops and laterally compete so that their diameter is enlarged (oblique walls) eliminating void networks [31]. Figure 1b shows how coherent grains are piled up to form the columns.

The PLT microstructure can be clearly described under the SZM model predictions [7] according to a regime of columnar uniform morphology ascribed to zone II, although our experimental T_s/T_m ratios ($T_s/T_m = 0.51-0.60$) correspond to the lowest limits for the appearance of a zone III morphology characterized by equiaxed grains. Such a microstructure reveals the existence of kinetic limitations beyond those imposed by the substrate temperature, which are likely to be connected to the kinetic energy losses of the incident particles during their collision with the deposition atmosphere. It has been suggested [7] that the development of a columnar compact microstructure is characterized by the formation of larger and uniform grains separated by more and more mobile boundaries as the film thickness increases. This results in a significant enhancement of the coarsening and coalescence of the grains, which improve the film crystallinity. The grain enlargement at increasing distances from the substrate surface can be verified in Figure 1b.

The columnar coarsening is mainly controlled by the grain coarsening, although some seldom evidences of column coalescence are observed. The column diameter (d) dependence on the deposition time (t), shown in Figure 2, was estimated by statistical studies from the cross-section SEM micrographs. The average columnar diameter evolves according to a power law relation, $d \sim t^{1/z}$. The coarsening exponents were obtained for PLT ($x = 0.08$) films grown on two different buffer layers: YSZ and CeO_2. In both cases, the deduced exponents $1/z$ (0.37 ± 0.07 for PLT/YSZ and 0.31 ± 0.08 for PLT/CeO_2) agree with those theoretically predicted for the morphological evolution of

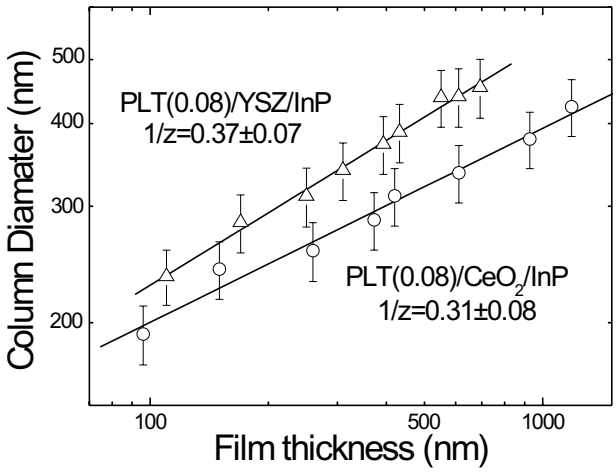

Fig. 2. Logarithmic plot of the columnar coarsening in PLT ($x = 0.08$) films deposited at $T_s = 923$ K in $PO_2 = 0.1$ mbar on Y-stabilized ZrO_2/InP ($\triangle$) and CeO_2/InP ($\circ$).

a growing surface destabilized by a non-local geometric shadowing effect ($1/z \sim 0.33$) [32].

Then, based on the SZM model, the developed microstructure appears as a result of the competition between two kinds of mechanisms: a non-local shadowing effect that destabilizes the growing surface, inducing the growth of 3D features (columns) and a local surface relaxation by the diffusion and/or evaporation/condensation (see below) which promotes the coarsening and grain coalescence. Neglecting any possible modification of the target morphology during the ablation process, the physical origin of the shadowing effects in PLD should be addressed to the interactions of the ablation plume with the deposition atmosphere [33]. The deposition gaseous pressure affects the angular distribution of the incident particles in two ways: i) by spatial confining of the plume promoting the collision between the ablated species, and ii) by direct collision with the oxygen molecules. Therefore, the high oxygen pressures broaden the angular distribution of

the incident particles originating a non-perpendicular incidence on the growing surface. As a result of the competition between surface features, the most prominent structures would shadow those located at more depressed surface regions and then, grow at a higher rate.

3.2 Growth spatial regimes

To separate the spatial scales in which each one of the involved mechanisms operates, the $PSDs(k)$ of the AFM images have been calculated and radially averaged by assuming an isotropic growing surface. Since in spite of the anisotropy of the local surface features, these appear randomly orientated and distributed over the surface (see below). According to the DST [34], for a L-sized system, $PSD(k)$ scales with growth time, t, and spatial frequency, k, as:

$$PSD(k,t) \propto k^{-(D+2\alpha)}\, f(k^z t),$$

such that for $x \gg 1$, $f(x) = const.$ and $PSD(k,t) \propto k^{-(D+2\alpha)}$. The dimension of the system is $D = 2$, and α is the roughness coefficient, representing the logarithmic spatial increase rate of the system saturated roughness: $w_{sat} \propto L^{\alpha}$.

The roughness coefficients corresponding to surface stabilization mechanisms have been predicted by several continuous and discrete 2D models. Thus, $\alpha = 0$ has been ascribed to surface relaxation by evaporation/condensation [5] (surface tension); $\alpha = 0.66$, to the relaxation by diffusion controlled by adsorption at kink sites [35] (including diffusion between kink sites); $\alpha = 1$, to relaxation by diffusion limited by the aggregation [36] (with irreversible kink absorption); and $\alpha = 1.5$ has been connected to relaxation by diffusion in faceted growth [37].

The calculated $PSDs(k)$ for PLT films of different La compositions deposited under several conditions are shown in Figure 3. Straight lines corresponding to $\alpha = 1$ and $\alpha = 0$ are also depicted to guide the regimes identification. In each curve, three regions can be separated by two crossovers, which are identified as the average grain size ($\xi_g \approx 50{-}120$ nm) and the average column diameter ($\xi_c \approx 300{-}500$ nm) respectively. The first regime with slope of ≈ -4 ($\alpha \approx 1$) reveals that the surface is laterally correlated by an atomic diffusion mechanism that operates at intragranular scale (lengths $< \xi_g$). This diffusion mechanism may drive the grain boundary migration and the grain coalescence in the columnar tops as well as inside the columns. In the second regime, a slope of ≈ -2 ($\alpha \approx 0$) points to a surface relaxation through an evaporation/condensation mechanism operating at intracolumnar scale ($\xi_g <$ lengths $< \xi_c$). This mechanism is controlled by the thermal reevaporation of the most volatile species (*i.e.* atomic Pb) that takes place during the growth and postdeposition annealing [38] promoted by the high substrate temperature and/or low oxygen pressure [25]. The presence of this mechanism suggests that the Pb losses by reevaporation occur in the highest positions of the growing surface, inhibiting the further growth in these sites. This fact is likely to be related to the difference in growth rate and thermal stability between PLT stoichiometric and non-stoichiometric phases. In the third regime (slope ≈ 0), the growing surface is laterally uncorrelated, therefore the $PSD(k)$ scaling ceases to be valid and the roughness coefficient is undefined. This regime is governed by a destabilizing mechanism operating at intercolumnar scale ($\xi_c <$ lengths). In agreement with the experimental data provided by SEM and described in the previous section, we can conclude that the mechanism operating in the third regime corresponds to a non-local shadowing effect [33]. Then, the $PSD(k)$ analysis carried out in generic PLT films confirms experimentally the SZM model predictions.

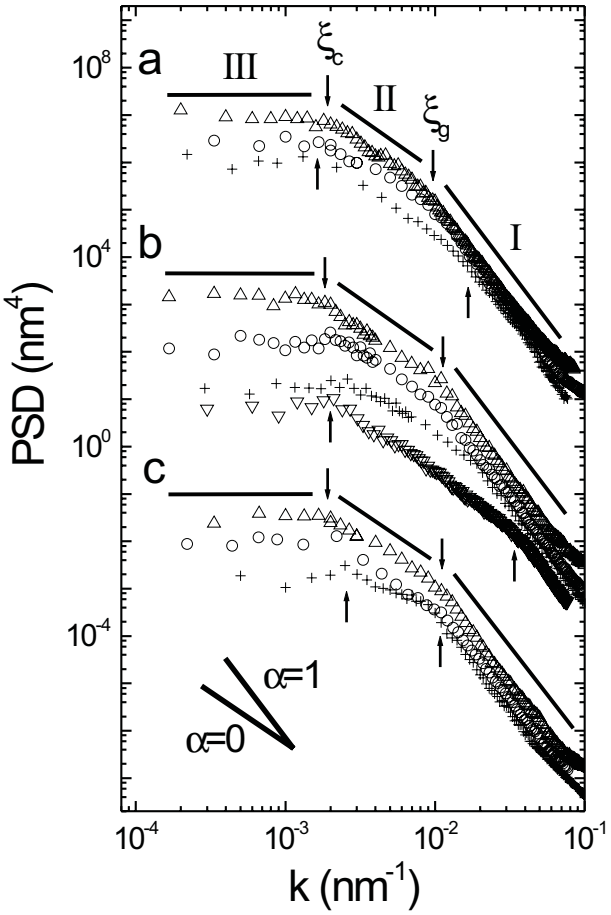

Fig. 3. $PSD(k)$ curves calculated from AFM images of 500 nm thick PLT films grown under several deposition parameters. a) Samples with different La compositions; $x = 0.08$ (+), $x = 0.15$ (○) and $x = 0.20$ (△) deposited on CeO_2/InP at $T_s = 923$ K in $PO_2 = 0.1$ mbar. b) Samples with a La composition of $x = 0.15$ deposited on YSZ/InP in $PO_2 = 0.1$ mbar at different temperatures; $T_s = 823$ K (▽), $T_s = 873$ K (+), $T_s = 923$ K (○) and $T_s = 973$ K (△). c) Samples with a La composition of $x = 0.08$ deposited on $SrTiO_3$/InP at $T_s = 923$ K in different oxygen pressures; $PO_2 = 0.05$ mbar (+), $PO_2 = 0.1$ mbar (○) and $PO_2 = 0.2$ mbar (△). The curves of series b and c have been shifted down, normalizing them by 10^4 and 10^8, respectively. Straight lines corresponding to $\alpha = 1$ and $\alpha = 0$ are depicted.

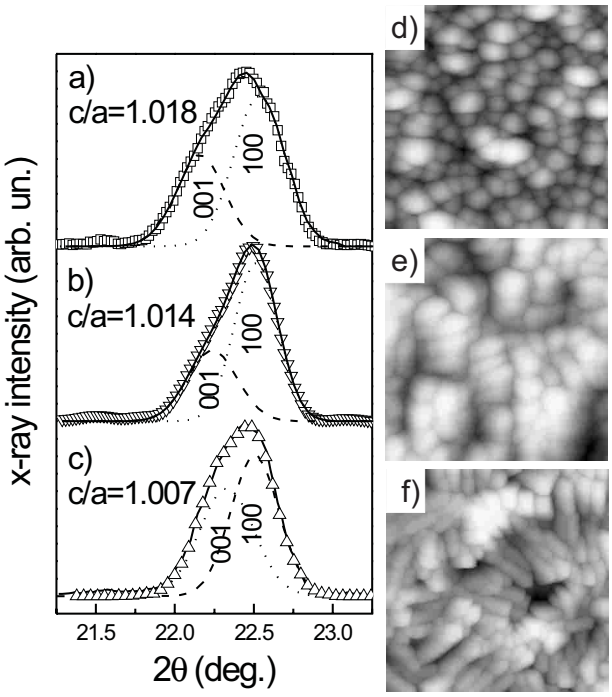

Fig. 4. 100/001 PLT X-ray peaks (left) and AFM images (right) of 500 nm thick PLT films with different La compositions; a) and d) $x = 0.08$, b) and e) $x = 0.15$, and d) and f) $x = 0.20$; deposited on $SrTiO_3$/InP at $T_s = 923$ K in $PO_2 = 0.1$ mbar. The unit-cell tetragonalities (c/a) are calculated from the 100/001 PLT deconvolutions also included in the graphs a), b) and c). The AFM images correspond to 1×1 μm^2 scanned areas.

3.3 Nanostructure

All the studied PLT films present a [001/100] preferential orientation independently of the used buffer layer. Within the angular range of $2\theta = 20°-80°$, XRD spectra exhibit the PLT 100/001 peak, their harmonics and very slight reminiscences of PLT [110] misorientation. A relevant region of XRD spectra, $2\theta = 21.2°-23.2°$, is shown in Figures 4a–c. The asymmetry of the PLT 100/001 peaks is due to the coexistence of two domains: an a-oriented domain responsible for the 100 diffraction, and a *c*-oriented 001 domain. The deconvolutions of the 100/001 PLT peaks in the two pseudo-Voight contributions for PLT films of different La compositions are shown in Figures 4a–c. The film unit-cell tetragonality (c/a) increases as the La concentration decreases ($c/a = 1.007$ for $x = 0.20$, $c/a = 1.014$ for $x = 0.15$ and $c/a = 1.018$ for $x = 0.08$) in agreement with the study made on ceramic PLT samples [14] (namely: $c/a = 1.013$ for $x = 0.20$, $c/a = 1.020$ for $x = 0.15$ and $c/a = 1.030$ for $x = 0.08$). The obtained values in our films are somewhat lower due to the stress induced in the PLT/buffer interface.

Figures 4d–f display an AFM image series of the PLT surface for increasing La concentration. These surfaces correspond to the column tops and exhibit smooth structures formed by groups of coherent grains. The surface roughness values are about 3−5% of the film thickness. As

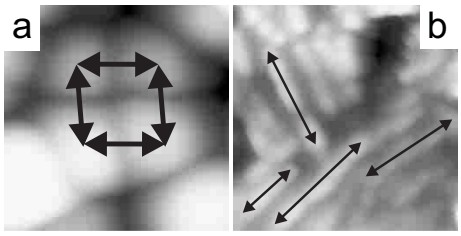

Fig. 5. AFM image magnifications: a) 190×190 nm^2 of the surface of 500 nm thick PLT(0.08)/$SrTiO_3$/InP deposited at $T_s = 923$ K in $PO_2 = 0.1$ mbar, and b) 300 nm thick 350×350 nm^2 of the surface of PLT(0.15)/Y-stabilized ZrO_2/InP deposited at $T_s = 923$ K in $PO_2 = 0.1$ mbar. Arrows point out the coalescence directions.

deduced above, at these spatial scales the diffusion mechanism rules the formation, coarsening and coalescence of the grains. Figure 5 reveals that for a low La concentration ($x = 0.08$) the grains coalesce isotropically (5a), while for a high La concentration ($x = 0.20$) the coalescence becomes anisotropic (5b). As a result of this difference, the PLT ($x = 0.08$) grains appear rounded (Fig. 4d) while the PLT ($x = 0.20$) grains develop tetragonal forms (Fig. 4f). The grain tetragonality increases as the unit-cell tetragonality decreases in forthright contradiction with the expected behavior, taking into account the tendency of the crystalline systems to approach the minimum energy shapes, which reflect the crystalline structure, as the diffusion is activated.

Figure 6 shows the dependence of the grain and unit-cell tetragonality with three experimental parameters: La composition, substrate temperature and dynamic oxygen pressure. The grain tetragonality values were estimated after averaging many measurements on individual grains. The statistics of procedure explains the relatively large error bars for these results. Figure 6a reproduces numerically the experimental evidences shown in Figure 4, *i.e.* the grain tetragonality increases with the La incorporation exhibiting an opposed behavior to that of unit-cell tetragonality. In the whole analyzed wide range of deposition conditions, the grain tetragonality increases as the substrate temperature increases or the oxygen pressure decreases while the unit-cell tetragonality remains quasi-constant. Slight unit-cell tetragonality deviations (enclosed in Figs. 6b and c) are induced by the stress enhancement as the grain size decreases. Small grains appear for very low deposition temperatures and/or high oxygen pressures. At this point, we look for common features in the grain tetragonality behavior with regard to the three modified experimental parameters. In order to keep the PLT molecule neutrality, the incorporation of x La atoms produces $x/2$ stoichiometric Pb vacancies ($\square$). On the other hand, it is well known the creation of non-stoichiometric Pb vacancies promoted by the increase of the substrate temperature and the decrease of the oxygen pressure *via* the thermal reevaporation of atomic Pb [25]. Based on the fact that the PLT film bulk is stoichiometric within the error ranges of X-ray photoelectron spectroscopy and Rutherford backscattering spectroscopy

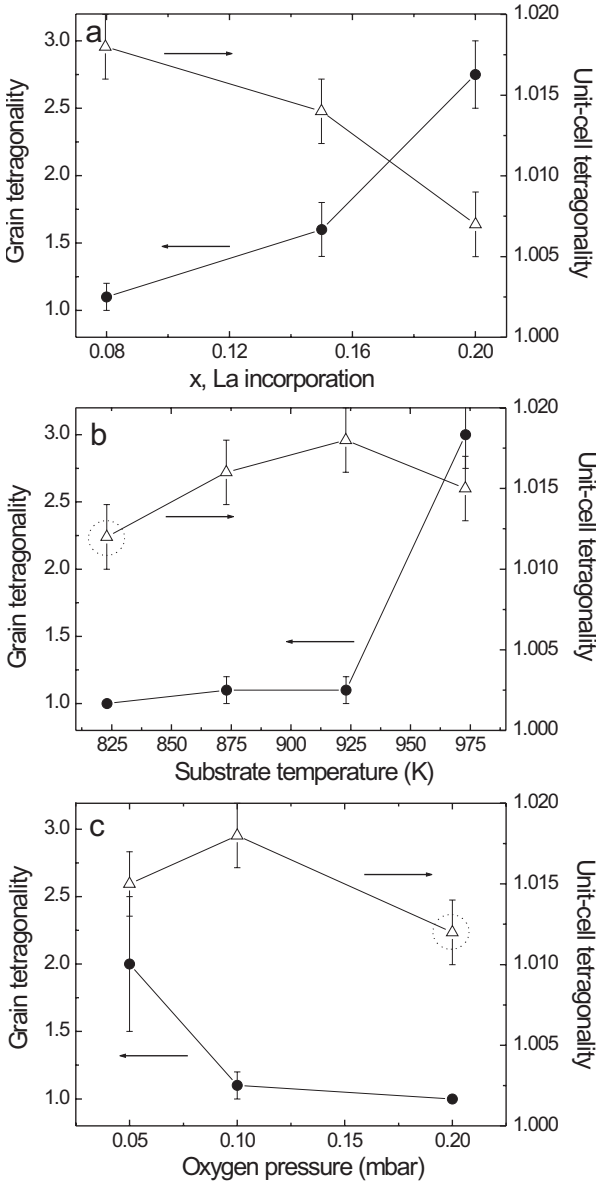

Fig. 6. Dependence of the grain (•) and unit-cell tetragonality (△) with: a) the La incorporation for PLT films deposited at T_s = 923 K in PO_2 = 0.1 mbar, b) the substrate temperature for PLT (x = 0.08) films deposited in PO_2 = 0.1 mbar, and c) the oxygen pressure during deposition of PLT (x = 0.08) films at T_s = 923 K. The PLT films, with thicknesses around 500±50 nm, were deposited on $SrTiO_3$/InP. The dot circles enclose slight deviations of the unit-cell tetragonality induced by the stress enhancement in the films.

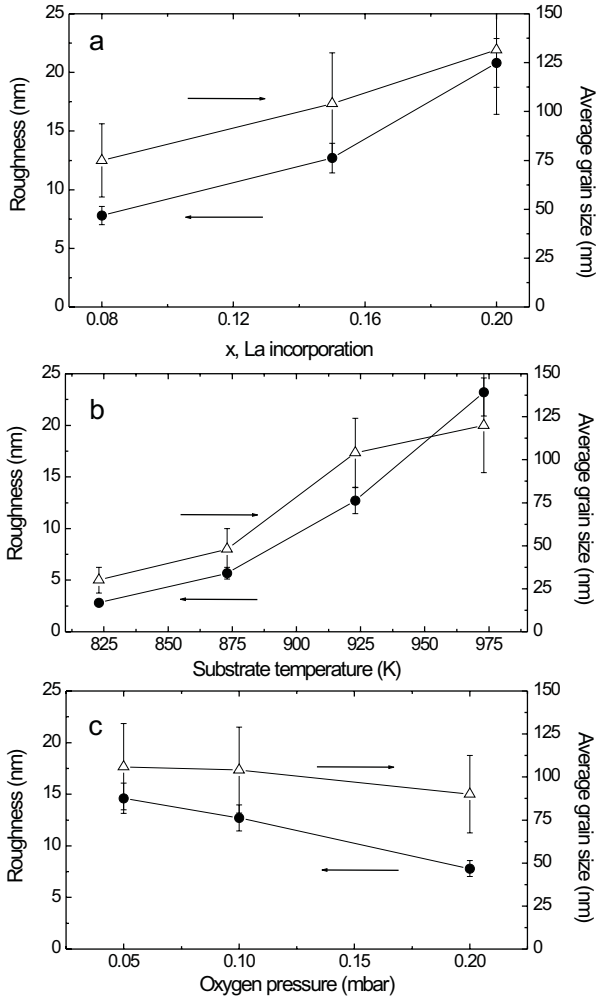

Fig. 7. Dependence of the film roughness (•) and the average grain size (△) with: a) the La incorporation for PLT films deposited at T_s = 923 K in PO_2 = 0.1 mbar, b) the substrate temperature for PLT (x = 0.15) films deposited in PO_2 = 0.1 mbar, and c) the oxygen pressure during deposition of PLT (x = 0.15) films at T_s = 923 K. The PLT films, with thicknesses around 500±50 nm, were deposited on $SrTiO_3$/InP.

techniques [24], it can be concluded that if there exists a concentration of non-stoichiometric Pb vacancies, it must be small and the vacancies should be strategically located at the grain boundaries. Such that the grain tetragonality could be associated with the fraction of stoichiometric and non-stoichiometric Pb vacancies in the PLT films, and therefore, the grain anisotropic coalescence could be the result of the self-alignment of Pb vacancies in preferential directions within PLT grains. Summarizing, the grain shape is not connected to the tetragonality of its unit-cell. This fact suggests that the minimum energy shapes of grains can be inhibited in compounds with highly volatile elements such as the modified-$PbTiO_3$ by the appearance of new kinetic barriers due to the onset of thermal evaporation.

Finally, Figure 7 shows how both the film roughness and the average grain size increase as the grain tetragonality increases. In the case of the non-equiaxed grains, the average grain size has been calculated as the average between the largest and the smallest grain lateral dimensions. The anisotropic coalescence hinders the obtaining of high crystalline (*i.e.* large grains) films with low roughness (< 3%). In order to overcome this drawback, a balance between roughness and crystallinity should be maintained for each application through a fine selection of the deposition parameters.

4 Conclusions

From the here-performed scaling analysis of the microstructure and morphology evolution of pulsed laser deposited PLT films, three growth mechanisms operating at different length scales have been identified: I) Atomic diffusion with grain boundary migration and grain coalescence at intragranular scale. II) Atomic evaporation/condensation at intracolumnar scale propitiated by thermal reevaporation of atomic Pb during the growth and the postdeposition annealing. III) Non-local shadowing effect promoting a compact columnar growth habit characterized by an uncorrelated growing surface at intercolumnar scale. The anisotropy nature of the atomic diffusion mechanism has been revealed and linked to the fraction of stoichiometric or non-stoichiometric Pb vacancies. The grains tetragonality is not linked to the tetragonality of its crystalline unit-cell, being inhibited the minimum energy shapes of grains.

References

1. (Optical scattering) D.K. Fork, F. Armani-Leplingard, J. Kingston. MRS Bull. **21**, 53 (1996); (Electron scattering) G. Palasantzas, Y.P. Zhao, G.C. Wang, T.M. Lu, J. Barnas, J.T.M. De Hosson, Phys. Rev. B **61**, 11109 (2002); (Phonon scattering) D.H. Santamore, M.C. Cross, Phys. Rev. B **66**, 144302 (2002)
2. (Strain relief) D.J. Srolovitz, Acta Metall. **37**, 621 (1989); G. Palasantzas, J. Th.M. De Hosson, Appl. Phys. Lett. **78**, 3044 (2001); (Carrier relaxation) T. Stirner, W.E. Hagston, M. Oneill, P. Harrison, J. Vac. Sci. Technol. B **12**, 1150 (1994)
3. (Molecular Beam Epitaxy) P. Tejedor, P. Smilauer, C. Roberts, B.A. Joyce, Phys. Rev. B **59**, 2341 (1999); (Sputtering) A.E. Lita, J.E. Sanchez, Phys. Rev. B **61**, 7692 (2000); (Chemical vapor deposition) F. Ojeda, R. Cuerno, R. Salvarezza, L. Vázquez, Phys. Rev. Lett. **84**, 3125 (2000)
4. F. Family, T. Vicsek, J. Phys. A **18**, L75 (1985); F. Family, Physica A **168**, 561 (1990)
5. A.L. Barabási, H.E. Stanley, *Fractal concepts in surface growth* (Cambridge University Press, Cambridge, 1995)
6. B.A. Movchan, A.V. Demchishin, Phys. Met. Metallogr. **28**, 83 (1969); R. Messier, J. Vac. Sci. Technol. A **4**, 490 (1986); C.C. Wong, H.I. Smith, C.V. Thompson, Appl. Phys. Lett. **48**, 335 (1986)
7. C.R.M. Grovenor, H.T.G. Hentzell, D.A. Smith, Acta Metall. **32**, 773 (1984)
8. J.A. Thornton, Annu. Rev. Mater. Sci. **7**, 239 (1977)
9. X. Zhu, G.C. Xiong, R. Liu, Y.J. Yi, G.J. Lian, Z.Z. Gan, J. Vac. Sci. Technol. B **12**, 2247 (1994); M.A. Harmer, C.R. Finsher, B.A. Parkinson, J. Appl. Phys. **70**, 2760 (1996); B. Dam, J.H. Rector, J.M. Huijbregtse, R. Griessen, Physica C **30**5, 1 (1998); J. Choi, C.B. Eom, G. Rijnders, H. Rogalla, D.H.A. Blank, Appl. Phys. Lett. **79**, 1447 (2001); S.K. Singh, M.R. Lees, R.K. Singh, S.B. Palmer, J. Phys. D Appl. Phys. **35**, 2243 (2002)
10. G.R. Fox, S.B. Krupanidhi, K.L. More, L.F. Allard, J. Mater. Res. **7**, 3039 (1992); Q. Gan, K. Wasa, C.B Eom, Mater. Sci. Eng. B **56**, 204 (1998); N. Wakiya, K. Kuroyanagi, Y. Xuan, K. Shinozaki, N. Mizutani, Thin Solid Film **357**, 166 (1999)
11. D. Dijkkamp, T. Venkatesan, X.D. Xu, S.A. Shaheen, N. Jisrawi, Y.H. Min-Lee, W.L. McCean, M. Croft, Appl. Phys. Lett. **51**, 619 (1987)
12. J.S. Horwitz, K.S. Grabowski, D.B. Chrisey, R.E. Leuchtner, Appl. Phys. Lett. **59**, 1565 (1991)
13. R. Von Helmot, J. Wecker, B. Holzapfel, L. Schultz, K. Samwer, Phys. Rev. Lett. **71**, 2331 (1994)
14. T. Yamamoto, H. Igarashi, K. Okazaki, J. Am. Ceram. Soc. **66**, 363 (1983)
15. H. Takeuchi, Cer. Bull. **71**, 974 (1992)
16. D. Garcia, J.A. Eiras, Ferroelectrics **123**, 51 (1991)
17. C. Wang, Y. Chen, M. Lee, C. Chiou, Y. Huang, Jpn J. Appl. Phys. **38**, 2831 (1999)
18. Y.M. Kang, S. Baik, J. Mat. Res. **13**, 995 (1999)
19. H. Adachi, T. Kawaguchi, K. Setsune, K. Ohji, K. Wasa, Appl. Phys. Lett. **42**, 867 (1983); Y. Shimizu. Jpn J. Appl. Phys. **32**, 2183 (1993)
20. Y. Tseng, K. Liu, J. Jiang, I. Lin, App. Phys. Lett. **72**, 3285 (1998)
21. G.M. Rao, S.B. Krupanidhi, Appl. Phys. Lett. **64**, 1591 (1994); H. Maiwa, N. Ichinose, Jpn J. Appl. Phys. **35**, 4976 (1996)
22. D. Pankaj, *Acusto-optic signal processing: fundamentals and applications* (Artech House Inc., USA, 1991), Chap. 5, pp. 171-292
23. *Pulsed Laser Deposition of Thin Films*, edited by D.B. Chrisey, G.K. Hubler (John Wiley and Sons, New York, 1994), Chaps. 14–16, pp. 20, 23
24. E. Vasco, O. Böhme, E. Román, C. Zaldo, A. Kling, M.F. Da Silva, Chem. Matt. **13**, 1061 (2001); E. Vasco, L. Vazquez, C. Zaldo, C. Coya, A. Kling, J.C. Soares, J. Vac. Sci. Technol. B **19**, 812 (2001); E. Vasco, C. Polop, C. Coya, A. Kling, C. Zaldo, Appl. Surf. Sci. **208**, 512 (2003)
25. J.S. Horwitz, K.S. Grabowski, D.B. Chrisey, R.E. Leuchtner, Appl. Phys. Lett. **59**, 1565 (1991)
26. R.F. C. Farrow, J. Phys. D **7**, L121 (1974)
27. G. Hollinger, E. Bergignat, J. Joseph, Y. Robach, J. Vac. Sci. Technol. A **3**, 2082 (1985)
28. Y. Shichi, S. Tanimoto, T. Goto, K. Kuroiwa, Y. Tarui, Jpn. J. Appl. Phys. **33**, 5172 (1994)
29. G.R. Bai, I.F. Tsu, A. Wang, C.M. Foster, C.E. Murray, V.P. Dravid, Appl. Phys. Lett. **72**, 1572 (1998) 1572; D.S. Eun, S.Y. Lee, Thin Solid Films **357**, 232 (1999)
30. B.W. Lee, L.P. Cook, P.K. Schenck, W. Wong-Ng, C.K. Chiang, P.S. Brody, K.W. Bennett, J. Mater. Res. **12**, 509 (1997)
31. G.S. Bales, A. Zangwill, J. Vac. Sci. Technol. A **9**, 145 (1991)
32. C. Roland, H. Guo, Phys. Rev. Lett. **66**, 2104 (1991); J.H. Yao, H. Guo, Phys. Rev. E **47**, 1007 (1993)
33. E. Vasco, C. Zaldo, L. Vázquez, J. Phys. Cond. Matt. **13**, L663 (2001)
34. W.M. Tong, R.S. Williams, Ann. Rev. Phys. Chem. **45**, 401 (1994)
35. Z.W. Lai, S.D. Sarma, Phys. Rev. Lett. **66**, 2348 (1991)
36. D.E. Wolf, J. Villain, Europhys. Lett. **13**, 389 (1990)
37. K. Fang, T.M. Lu, G.C. Wang, Phys. Rev. B **49**, 833 (1994)
38. E. Vasco, O. Böhme, E. Román, C. Zaldo, Appl. Phys. Lett. **78**, 2037 (2001)